Supplementary Information for

Role of the energy offset on the charge photogeneration and voltage loss of nonfullerene acceptor-based organic solar cells

Yasunari Tamai,*[a,b] Rei Shirouchi,[a] Toshiharu Saito,[a] Kazuki Kohzuki,[a] and Shin-ichiro Natsuda[a]

[a] Department of Polymer Chemistry, Graduate School of Engineering, Kyoto University, Katsura, Nishikyo, Kyoto 615-8510, Japan

[b] Japan Science and Technology Agency (JST), PRESTO, 4-1-8 Honcho Kawaguchi, Saitama 332-0012, Japan

*Corresponding author: tamai@photo.polym.kyoto-u.ac.jp

Experimental details

Materials: All donors were purchased from Solarmer Energy, Inc., whereas all acceptors were purchased from 1-Material, Inc. All materials were used as received.

Device fabrication: The photovoltaic devices were fabricated on ITO/glass substrates (Geomatec Co., 1006, 10 Ω sq.$^{-1}$), which were cleaned by sonication consecutively in toluene, acetone, and ethanol, followed by UV-O_3 treatment (Nippon Laser and Electronics Lab.) for 30 min. PEDOT:PSS (Clevios, AI4083) was spin-coated onto the substrates and dried on a hot plate under ambient condition. Thereafter, active layers were spin-coated onto the substrates in a N_2-filled glovebox (see Tables S1–S3). Subsequently, PDINO or PNDIT-F3N-Br were spin-coated from methanol solution, and 100 nm of Al or Ag were thermally evaporated thereon. The devices were encapsulated in the glovebox using a UV curable epoxy for the EL measurements, while they were set in a N_2-filled chamber for the *J–V* and EQE_{PV} measurements. On the other hand, the samples for the optical measurements were prepared on quartz substrates.

J–V and EQE_{PV} measurements: The *J–V* characteristics were measured using a DC voltage and current source/monitor (Keithley, 2611B) in a dark and under AM1.5G simulated solar illumination at 100 mW cm^{-2}. The light intensity was corrected with a calibrated Si photodiode (Bunko-Keiki, BS-520). The EQE_{PV} spectra were measured with a spectral response measurement system (Bunko-Keiki, ECT-25D).

Steady-state absorption, PL and EL measurements: UV–visible absorption spectra were measured using a UV–visible spectrometer (Hitachi, U-4100). PL spectra were measured using a PL spectrometer (Horiba Jobin Yvon, Nanolog) equipped with a photomultiplier tube (Hamamatsu, R928P) and a liquid-N_2-cooled InGaAs near-IR array detector (Horiba Jobin Yvon, Symphony II). EQE_{EL} were measured using an absolute QY measurement system (Bunko-keiki, BEL-300) with an integrating sphere. A DC voltage and current source/monitor (Advantest, R-6243) was used to adjust the applied voltage.

TA measurements: TA data were collected using a pump and probe femtosecond TA spectroscopy system, which consisted of a TA spectrometer (Ultrafast Systems, Helios) and a regenerative amplified Ti:sapphire laser (Spectra-Physics, Hurricane). A fundamental pulse with a wavelength of 800 nm was used as the excitation source for NFAs. The TA data were collected over a time range from −5 ps to 3 ns.

PYSA measurements: The IEs were measured using a photoelectron yield spectrometer (Riken Keiki, AC-3) with a power setting of 5 nW. Calibration was performed using an Au layer. All films were prepared on ITO/glass substrates. The threshold energy for the photoelectron emission was evaluated based on the cubic root of the photoelectron yield plotted against the incident photon energy.

Table S1. Fabrication conditions for PBDB-T-based devices.

Acceptor	Solvent[a]	Concentration (mg mL^{-1})	D:A ratio	Annealing
Y1	CF/CN	17.6	1:1.2	110 °C, 5 min
Y2	CF/CN	17.6	1:1.2	110 °C, 5 min
Y5	CF/CN	17.6	1:1.2	110 °C, 5 min
Y6	CF/CN	17.6	1:1.2	110 °C, 5 min
Y6N3	CF/CN	17.6	1:1.2	110 °C, 5 min
Y12	CF/CN	17.6	1:1.2	110 °C, 5 min
Y16	CF/CN	17.6	1:1.2	110 °C, 5 min
L8-BO	CF/DIO	15.4	1:1.2	100 °C, 10 min

[a]: CF/CN: chloroform mixed with 1-chloronaphthalene (0.5 vol.%), and CF/DIO: chloroform mixed with 1,8-diiodooctane (0.25 vol.%).

Table S2. Fabrication conditions for PBDB-T-2F-based devices.

Acceptor	Solvent[a]	Concentration (mg mL^{-1})	D:A ratio	Annealing
Y1	CF/CN	17.6	1:1.2	110 °C, 5 min
Y2	CF/CN	16	1:1	110 °C, 5 min
Y5	CF/CN	17.6	1:1.2	110 °C, 5 min
Y6	CF/CN	17.6	1:1.2	110 °C, 5 min
Y6N3	CF/CN	17.6	1:1.2	110 °C, 5 min
Y12	CF/CN	17.6	1:1.2	110 °C, 5 min
Y16	CF/CN	16	1:1	110 °C, 5 min
L8-BO	CF/DIO	15.4	1:1.2	100 °C, 10 min

[a]: CF/CN: chloroform mixed with 1-chloronaphthalene (0.5 vol.%), and CF/DIO: chloroform mixed with 1,8-diiodooctane (0.25 vol.%).

Table S3. Fabrication conditions for PBDB-T-2Cl-based devices.

Acceptor	Solvent[a]	Concentration (mg mL^{-1})	D:A ratio	Annealing
Y1	CF/CN	17.6	1:1.2	110 °C, 5 min
Y2	CF/CN	17.6	1:1.2	110 °C, 5 min
Y5	CF/CN	17.6	1:1.2	110 °C, 5 min
Y6	CF/CN	17.6	1:1.2	110 °C, 5 min
Y6N3	CF/CN	17.6	1:1.2	110 °C, 5 min
Y12	CF/CN	17.6	1:1.2	110 °C, 5 min
Y16	CF/CN	16	1:1	110 °C, 5 min
L8-BO	CF/DIO	15.4	1:1.2	100 °C, 10 min

[a]: CF/CN: chloroform mixed with 1-chloronaphthalene (0.5 vol.%), and CF/DIO: chloroform mixed with 1,8-diiodooctane (0.25 vol.%).

Absorption spectra of pristine donor and acceptor films

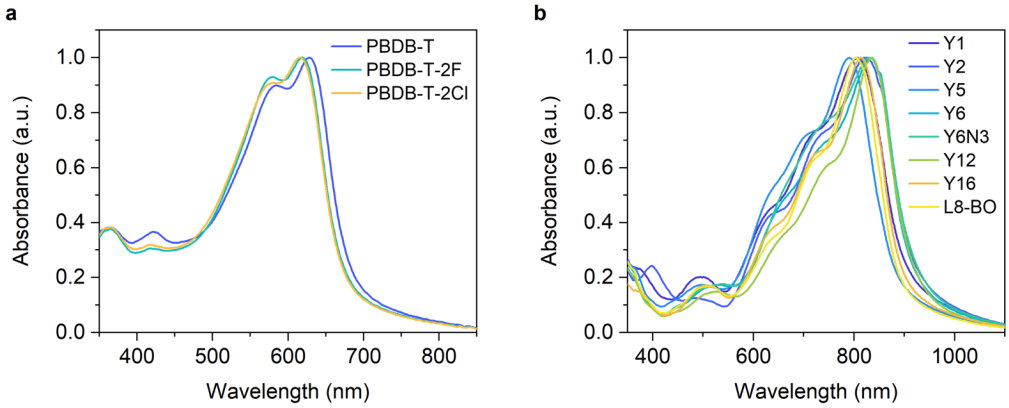

Figure S1. Absorption spectra of pristine **a** donor and **b** acceptor films.

Ionization energy

Figure S2 shows the IEs of the materials employed in this study in their pristine film state. These values are consistent with previously reported values.[S1] Figure S3a shows the correlation between the IEs presented in this study and those reported in ref. S1 (IE_{ref}). The Pearson correlation coefficient r was 0.98, indicating a strong positive correlation between IEs and IE_{ref}s, while a small systematic error was observed between these values. The dashed line represents the best fitting curve obtained using the following linear equation: $IE_{ref} = \alpha \times IE + \beta$ with $\alpha = 1.00$ and $\beta = -0.14$. In contrast, the small systematic error did not affect our conclusion because it was compensated when the IE difference was calculated; the differences between the IEs of the donor and acceptor materials evaluated in this study were almost identical to those reported in ref. S1 ($r = 0.96$, Figure S3b).

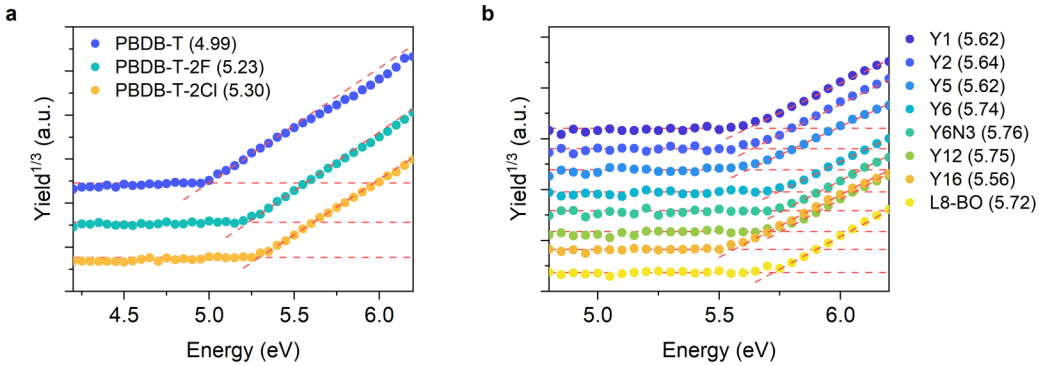

Figure S2. Photoelectron yield spectra of **a** donor and **b** acceptor materials in their pristine film states measured in air. Values in parenthesis are the IEs evaluated from the onset energy based on the cubic root of the photoelectron yield plotted against the incident photon energy (unit: eV). All measurements were conducted five times, and the IEs were the average values of the five measurements.

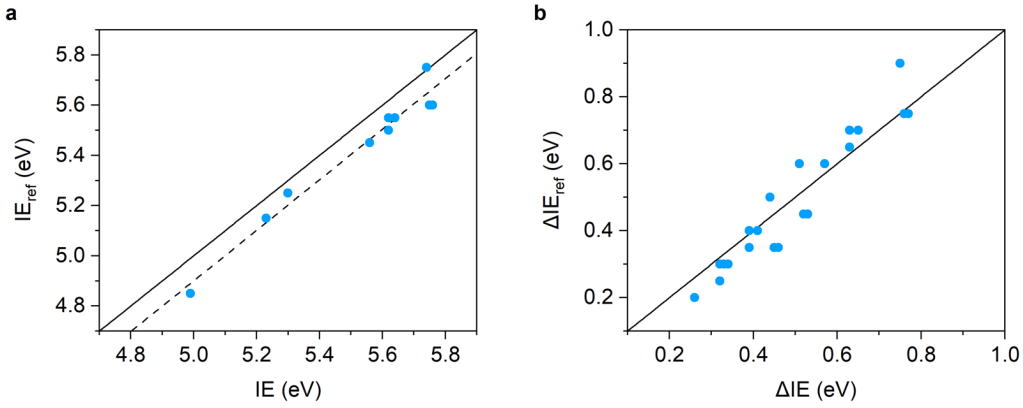

Figure S3. Correlations between **a** IEs and IE_{ref}s and **b** ΔIEs and ΔIE_{ref}s measured by PYSA. Note that the data of L8-BO were not plotted because it was not reported in ref. S1.

LUMO energy

Figures S4a and S4b show the photoluminescence (PL) spectra of the materials in their pristine film state. The excited-state energies E_S were determined at the intersection between the absorption (Figure S1) and PL spectra. The LUMO energies were estimated using the IEs and E_S (Figure S4c).

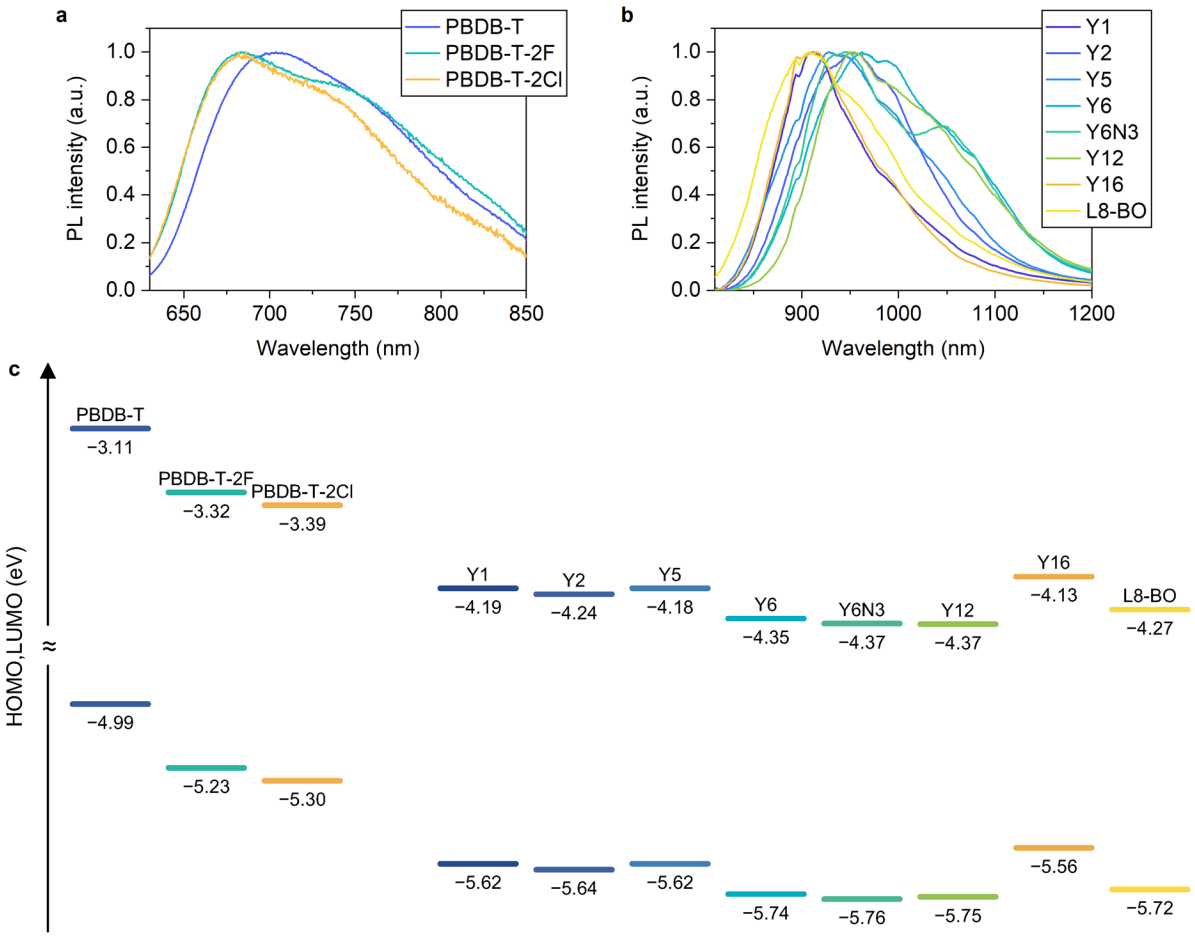

Figure S4. PL spectra of pristine **a** donor and **b** acceptor films. **c** The HOMO and LUMO energies. The HOMO energies were evaluated by PYSA (Figure S2), whereas the LUMO energies were calculated as the sum of the HOMO energies and E_S.

J–V characteristics

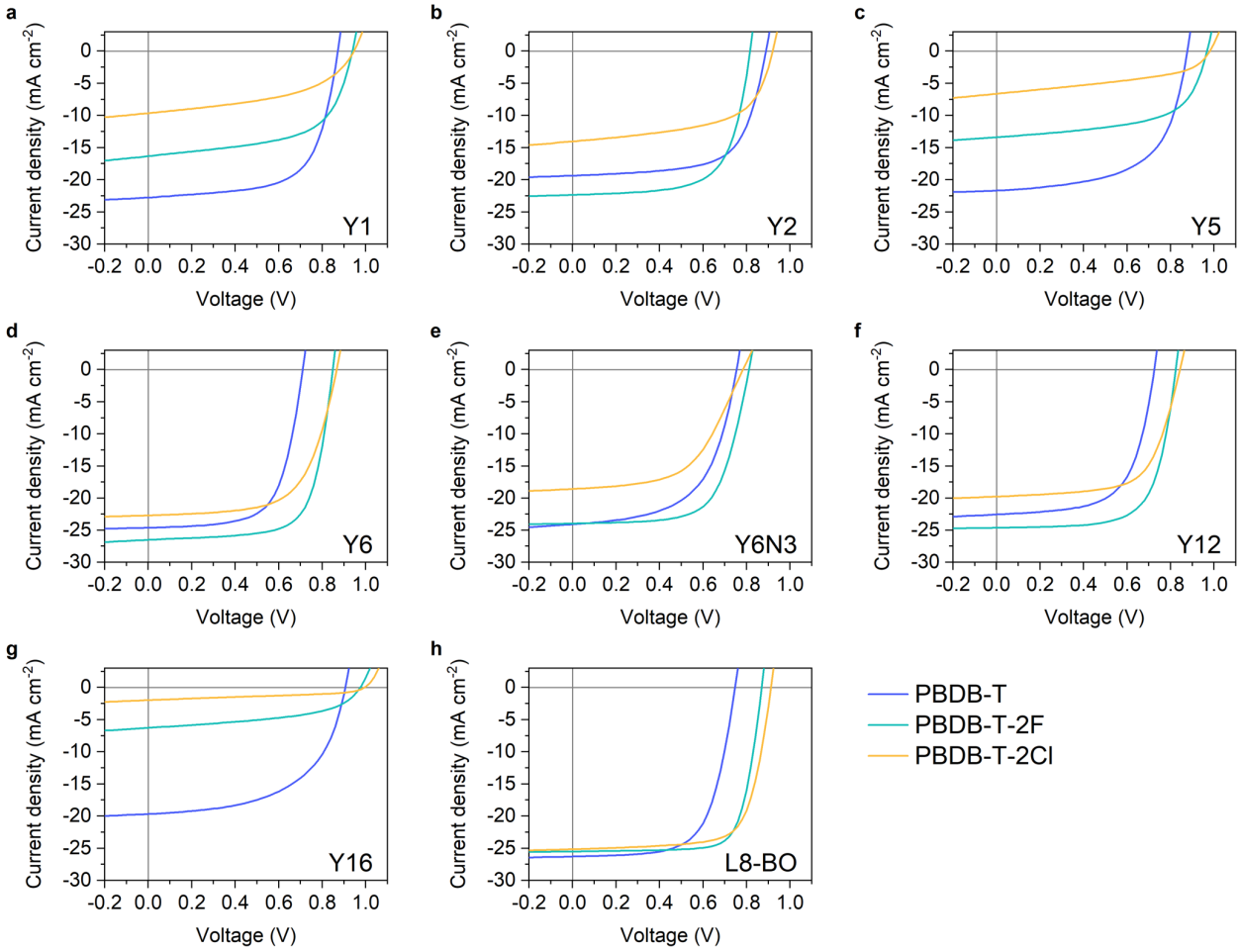

Figure S5. *J–V* characteristics: **a** Y1, **b** Y2, **c** Y5, **d** Y6, **e** Y6N3, **f** Y12, **g** Y16, and **h** L8-BO based devices. A part of the experimental data presented in this study were obtained from our previous study.[S2]

EQE_{PV} spectra

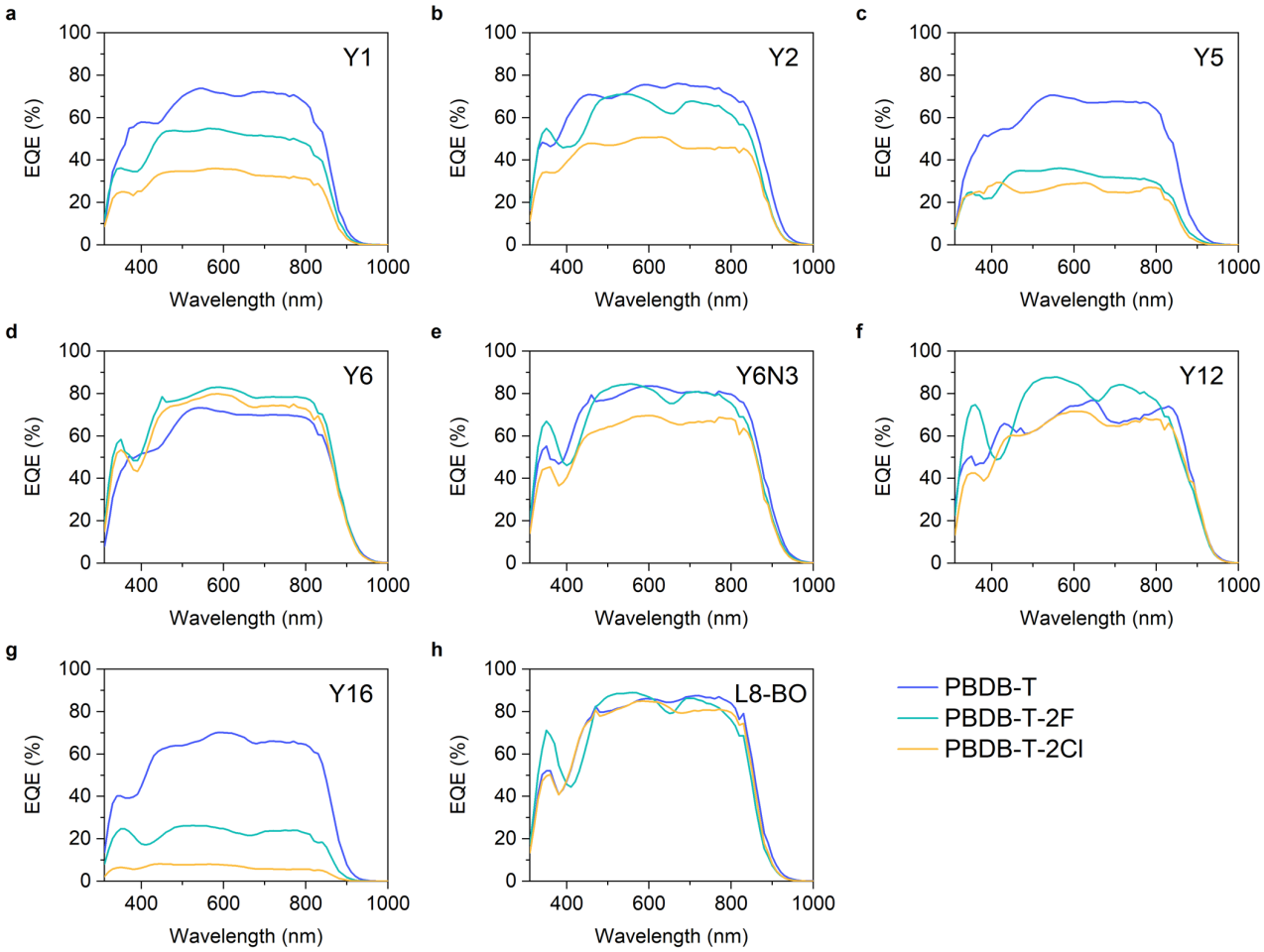

Figure S6. EQE_{PV} spectra: **a** Y1, **b** Y2, **c** Y5, **d** Y6, **e** Y6N3, **f** Y12, **g** Y16, and **h** L8-BO based devices. A part of the experimental data presented in this study were obtained from our previous study.[S2]

Table S4. Device parameters for PBDB-T-based devices.

Acceptor	J_{SC} (mA cm^{-2})	$J_{SC}^{calc.\ a}$ (mA cm^{-2})	V_{OC} (V)	FF	PCE (%)
Y1	22.59	21.38	0.868	0.638	12.51
Y2	21.83	23.39	0.814	0.652	11.59
Y5	20.69	20.14	0.873	0.587	10.59
Y6	24.78	21.86	0.707	0.596	10.43
Y6N3	23.58	25.53	0.746	0.560	9.86
Y12	21.73	22.78	0.733	0.620	9.87
Y16	19.32	20.35	0.902	0.555	9.68
L8-BO	26.28	25.62	0.754	0.661	13.11

[a]: J_{SC} calculated by integrating the EQE_{PV} spectra.

Table S5. Device parameters for PBDB-T-2F-based devices.

Acceptor	J_{SC} (mA cm^{-2})	$J_{SC}^{calc.\ a}$ (mA cm^{-2})	V_{OC} (V)	FF	PCE (%)
Y1	15.10	15.85	0.938	0.549	7.82
Y2	19.16	20.56	0.890	0.654	11.14
Y5	11.97	9.97	0.964	0.574	6.65
Y6	25.42	24.99	0.840	0.698	14.90
Y6N3	24.10	24.77	0.812	0.660	12.90
Y12	23.56	25.39	0.823	0.687	13.33
Y16	6.18	7.32	0.973	0.489	2.94
L8-BO	25.96	24.85	0.864	0.733	16.42

[a]: J_{SC} calculated by integrating the EQE_{PV} spectra.

Table S6. Device parameters for PBDB-T-2Cl-based devices.

Acceptor	J_{SC} (mA cm^{-2})	$J_{SC}^{calc.\ a}$ (mA cm^{-2})	V_{OC} (V)	FF	PCE (%)
Y1	9.68	10.36	0.949	0.488	4.49
Y2	14.25	15.25	0.918	0.575	7.53
Y5	6.62	8.15	0.981	0.439	2.85
Y6	22.53	23.60	0.865	0.629	12.26
Y6N3	19.27	21.03	0.797	0.555	8.53
Y12	18.21	21.50	0.831	0.627	9.54
Y16	1.93	2.13	0.992	0.402	0.77
L8-BO	24.78	24.53	0.913	0.722	16.33

[a]: J_{SC} calculated by integrating the EQE_{PV} spectra.

Energy transfer

Figure S7 shows the PL spectra of PBDB-T-2F:Y5 blend and pristine PBDB-T-2F films after photoexcitation at 600 nm (PBDB-T-2F excitation). The PL band in the 600–800 nm region attributable to the PBDB-T-2F fluorescence (blue line) was completely quenched in the blend film. Instead, a large PL band, similar to the Y5 fluorescence, was observed in the 800–1200 nm region only in the blend film. These results indicate that the energy transfer from PBDB-T-2F to Y5 kinetically outcompetes the electron transfer.

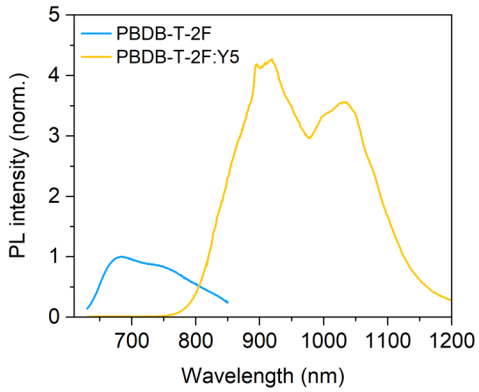

Figure S7. PL spectra of the PBDB-T-2F:Y5 blend and pristine PBDB-T-2F films after photoexcitation at 600 nm. The excitation fluence and the detection conditions were the same for the two spectra.

Threshold value of ΔIE_{PYSA}

As many previous studies have reported the plots of EQE_{PV} against ΔIE, herein, we also plotted EQE_{PV} against ΔIE_{PYSA}, as shown in Figure S8a. The threshold value of ΔIE_{PYSA} that ensured efficient charge photogeneration was ~0.42 eV.

The red solid line in Figure S8a represents the best fitting curve obtained using the following equation proposed in ref. S3:

$$EQE_{PV} = \alpha\left(1 + \mathrm{erf}\frac{\Delta IE - \beta}{\gamma}\right) \quad (S1)$$

where α, β, and γ are the fitting parameters and "erf" refers to the error function. The EQE_{PV} data can be well fitted using Eq. S1 with β of 342 meV and γ of 98 meV. These values are in agreement with those reported in ref. S3, where β was considered a bias potential induced by charge–quadrupole interactions. However, we stress that as a step-like dataset can usually be adequately fitted using an error function, the suitable fit achieved using Eq. S1 does not necessarily imply that β represents the amount of band bending required for efficient charge separation. For example, Eq. S1 also provides an appropriate fit for the EQE_{PV} of fullerene-based OSCs (Figure S9), despite negligible quadrupole moments of fullerenes. In addition, as shown in Figure S8b, Eq. S1 did not afford a suitable fit for the PL quenching yield Φ_q (in ref. S6, the decrease in EQE_{PV} below the threshold was attributed to a decrease in Φ_q due to the bias potential being larger than ΔIE). Instead, the EQE_{PV} / Φ_q could be appropriately fitted using Eq. S1 (Figure S8c).

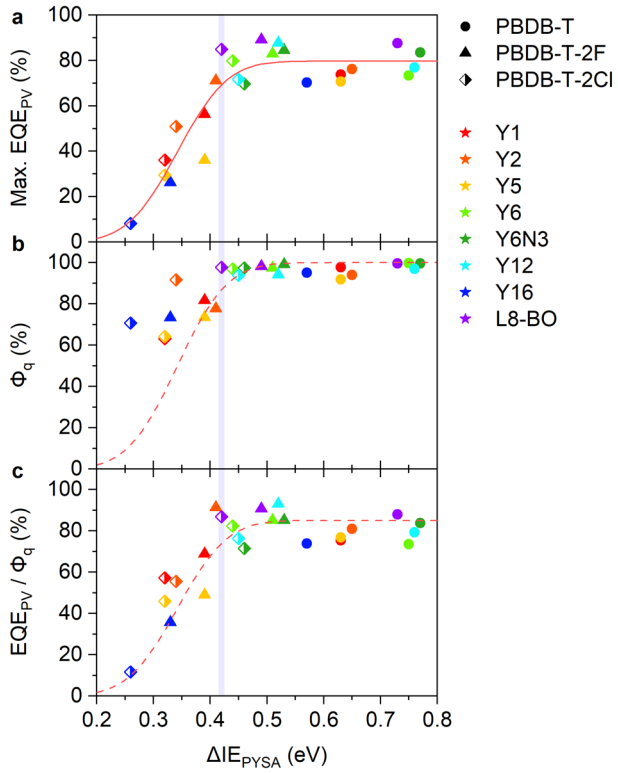

Figure S8. **a** Maximum EQE$_{PV}$, **b** PL quenching yield Φ_q, and **c** EQE$_{PV}$ / Φ_q plotted against ΔIE_{PYSA}. The red solid line in panel **a** represents the best fitting curve obtained using Eq. S1 with β of 342 meV and γ of 98 meV. The red dashed lines in panels **b** and **c** are the best fitting curves obtained using Eq. S1, where β and γ were fixed to the abovementioned values.

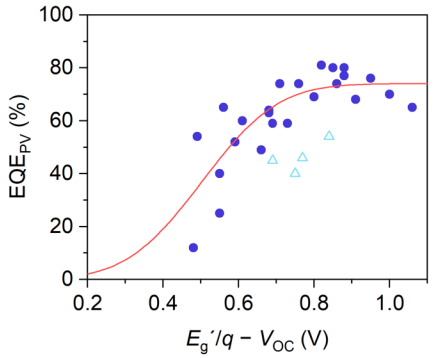

Figure S9. Maximum EQE$_{PV}$ of fullerene-based OSCs plotted against $E_g'/q - V_{OC}$. The red solid line represents the best fitting curve obtained using Eq. S1 with β of 503 meV and γ of 224 meV. The data used in this plot were obtained from previous reports.[S4-S26] Open triangles were not included in the fitting.

Threshold value of ΔV

As shown in Figure 2d in the main text, the threshold value of ΔV for efficient charge photogeneration was ~0.52 V. In this study, E_g was determined from the EQE_{PV} spectra using the method proposed earlier.[S27] On the other hand, in the old papers (and still sometimes), E_g was determined from the absorption onset. Therefore, we also determined the optical bandgap from the absorption onset (herein denoted E_g' to distinguish it from the E_g determined by the criterion we adopted in this study) and compared the threshold value with that of fullerene-based OSCs. Figure S10 shows the maximum EQE_{PV} plotted against $E_g'/q - V_{OC}$. The threshold value was determined to be ~0.5 V, which was lower than that of the fullerene-based OSCs (0.6 V).[S4,S5]

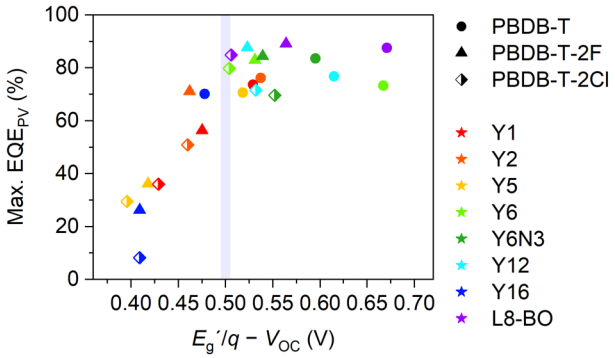

Figure S10. Maximum EQE_{PV} plotted against $E_g'/q - V_{OC}$.

Evaluation of voltage losses

When evaluating the voltage loss, the EQE_{PV} spectra were extended to lower energies using EL spectra according to the procedure reported previously.[S28] V_{OC} can be divided into several components, as follows[S27]

$$V_{\mathrm{OC}} = \frac{E_{\mathrm{g}}}{q} - \Delta V_{\mathrm{SQ}} - \Delta V_{\mathrm{SC}} - \Delta V_{\mathrm{r}} - \Delta V_{\mathrm{nr}} = V_{\mathrm{OC}}^{\mathrm{rad}} - \Delta V_{\mathrm{nr}} \quad \text{(S2).}$$

ΔV_{SQ} is the voltage loss due to unavoidable radiative charge recombination given as:

$$\Delta V_{\mathrm{SQ}} = \frac{E_{\mathrm{g}}}{q} - V_{\mathrm{OC}}^{\mathrm{SQ}} \quad \text{(S3)}$$

where V_{OC}^{SQ} is the maximum achievable V_{OC} for an ideal solar cell within the SQ framework, of which EQE_{PV} is unity (zero) above (below) E_g. V_{OC}^{SQ} is given as:

$$V_{\mathrm{OC}}^{\mathrm{SQ}} = \frac{k_{\mathrm{B}}T}{q} \ln\left(\frac{J_{\mathrm{SC}}^{\mathrm{SQ}}}{J_0^{\mathrm{SQ}}}\right) \quad \text{(S4)}$$

with

$$J_{\mathrm{SC}/0} = q \int_0^{\infty} \mathrm{EQE}_{\mathrm{PV}}(E)\, \emptyset_{\mathrm{AM1.5G/BB}}(E) \mathrm{d}E \quad \text{(S5)}$$

where $\emptyset_{\mathrm{AM1.5G}}$ is the AM1.5G solar spectrum, whereas $\emptyset_{\mathrm{BB}}$is the blackbody emission flux density from the device.

ΔV_{SC} is the voltage loss due to the imperfection in EQE_{PV} of the real OSCs above the E_g region, given as:

$$\Delta V_{\mathrm{SC}} = -\frac{k_{\mathrm{B}}T}{q} \ln\left(\frac{J_{\mathrm{SC}}}{J_{\mathrm{SC}}^{\mathrm{SQ}}}\right) \quad \text{(S6).}$$

ΔV_r is the nonideal, extra radiative voltage loss associated with the photocurrent response in the region below E_g given as

$$\Delta V_{\mathrm{r}} = -\frac{k_{\mathrm{B}}T}{q} \ln\left(\frac{J_0^{\mathrm{SQ}}}{J_0^{\mathrm{r}}}\right) \quad \text{(S7).}$$

ΔV_{nr} is obtained from the difference between ΔV and $\Delta V_{SQ} + \Delta V_{SC} + \Delta V_r$.

Table S7. V_{OC}^{rad} for OSC devices.

Acceptor\Donor	PBDB-T	PBDB-T-2F	PBDB-T-2Cl
Y1	1.114	1.120	1.123
Y2	1.079	1.092	1.094
Y5	1.107	1.109	1.131
Y6	1.070	1.084	1.087
Y6N3	1.079	1.073	1.084
Y12	1.076	1.078	1.059
Y16	1.120	1.126	1.131
L8-BO	1.111	1.120	1.122

unit: V

Table S8. ΔV_{nr} for OSC devices.

Acceptor\Donor	PBDB-T	PBDB-T-2F	PBDB-T-2Cl
Y1	0.246	0.181	0.174
Y2	0.265	0.202	0.176
Y5	0.234	0.145	0.150
Y6	0.363	0.244	0.222
Y6N3	0.333	0.261	0.287
Y12	0.343	0.255	0.228
Y16	0.218	0.153	0.139
L8-BO	0.357	0.256	0.209

unit: V

EQE_{EL}

Figures S11a and S11b show the EL spectra of PBDB-T-2F:Y5 and PBDB-T-2F:Y6 devices. Average EQE_{EL}s were determined to be 3.0×10^{-3} and 8.0×10^{-5} for PBDB-T-2F:Y5 and PBDB-T-2F:Y6 devices, respectively (Figure S11c). The corresponding $\Delta s V_{nr}$s calculated using Eq. S8 were 0.151 and 0.245 V, respectively (T was set to 296 K).

$$\Delta V_{\mathrm{nr}} = -\frac{k_{\mathrm{B}}T}{q}\ln(\mathrm{EQE_{EL}}) \qquad \text{(S8)}.$$

These values were in good agreement with those determined by the EQE_{PV}s (Table S8). Therefore, we used ΔV_{nr} determined by EQE_{PV} for the main discussion because of considerable uncertainties in EQE_{EL}s for some large energy offset systems due to the limitation of the sensitivity of our equipments.

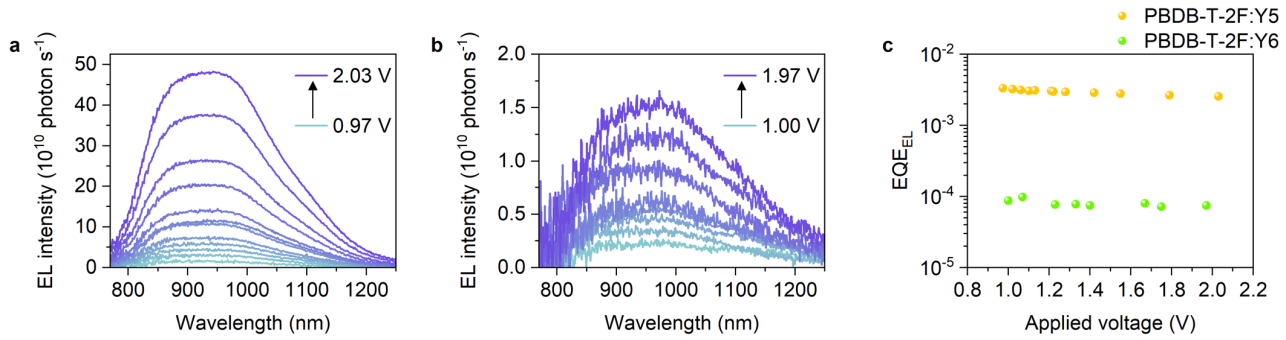

Figure S11. EL spectra of **a** PBDB-T-2F:Y5, and **b** PBDB-T-2F:Y6 devices at forward biases. **c** EQE_{EL} plotted against applied voltage.

ΔV_{nr} v.s. ΔV

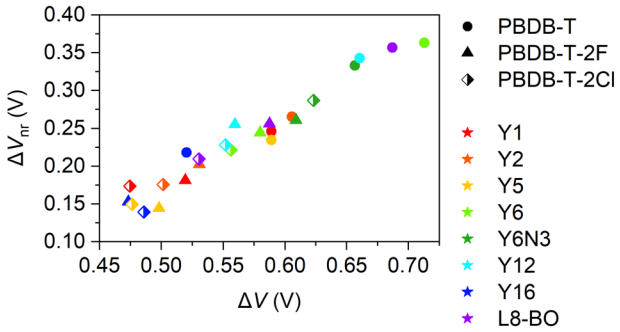

Figure S12. ΔV_{nr} plotted against ΔV.

PL quenching yield

Figure S13 shows the PL spectra of the blend films after photoexcitation at 800 nm (acceptor excitation). The PL quenching yields (Φ_qs) were determined as the PL intensity ratio between the blend and pristine acceptor films as follows

$$\Phi_q = 1 - \frac{\int_0^\infty \mathrm{PL}_{\mathrm{blend}}(E)\,\mathrm{d}E}{\int_0^\infty \mathrm{PL}_{\mathrm{pristine}}(E)\,\mathrm{d}E} \tag{S9}$$

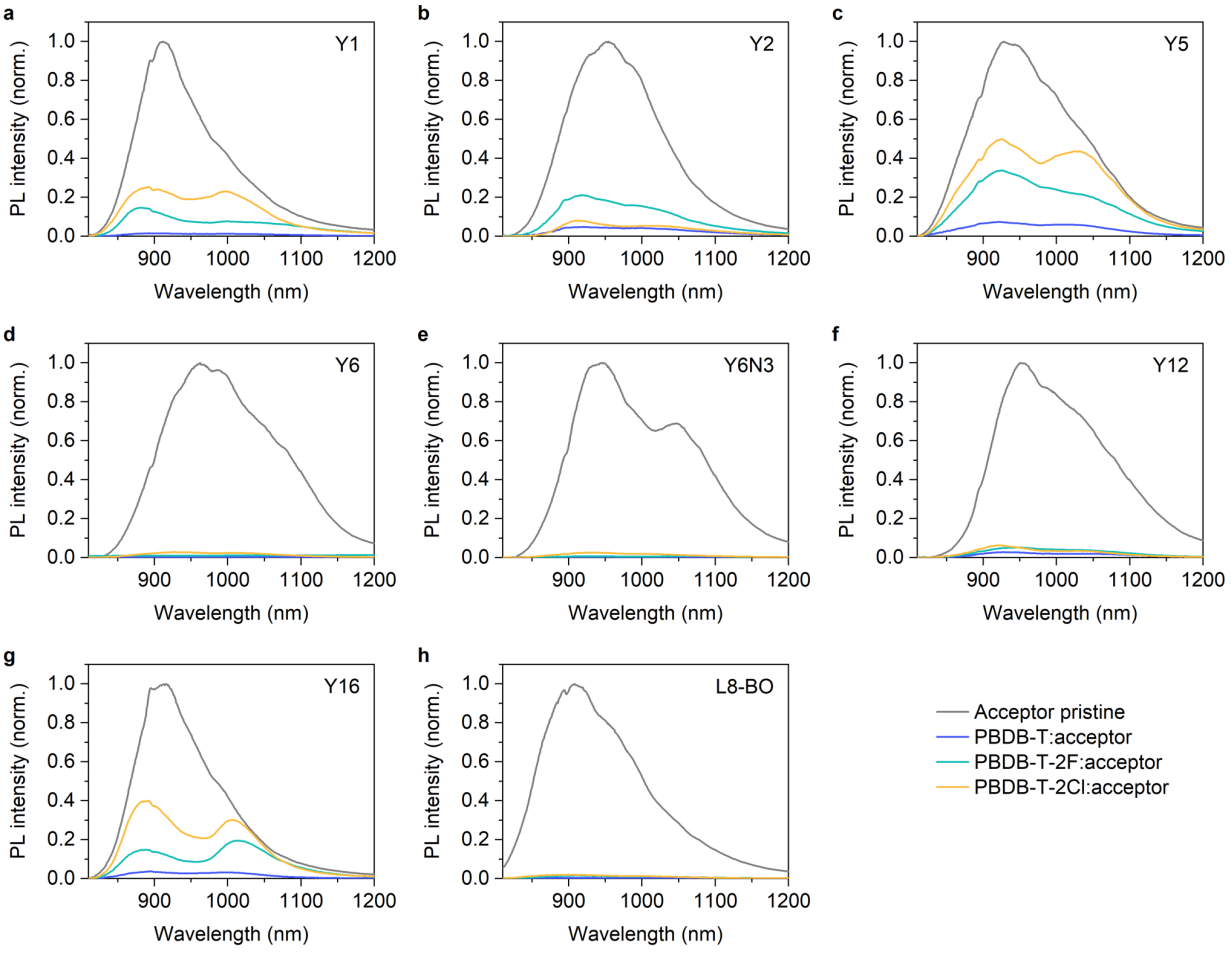

Figure S13. PL spectra of D:A blend films and corresponding pristine acceptor films. PL intensities of the blend films and corresponding pristine films were corrected for differences in absorbance at the excitation wavelength and normalized such that the peak PL intensity of the pristine film was 1.

Figure S14 shows the PL quenching yield Φ_q plotted against ΔV_{nr}. Note that the data presented in this figure is different from that provided in Figure 3b, as explained below. In Figure S14, Φ_qs of some blend films were relatively low. A close inspection of the PL spectra of these films revealed that, in addition to the emission

from local excited (LE) states peaking at 850–950 nm depending on the acceptor, an extra PL band, which was not observed in corresponding pristine films, was observed on the lower energy side. Based on time-resolved PL spectroscopy, the lower-energy PL band is attributed to the CT emission.[S29] As we needed the quenching yields corresponding to the LE band in this study, the PL spectra were decomposed into two Gaussian bands, representing the LE and CT parts, when Φ_q determined by the PL intensity of the entire spectrum was less than 60%. Note that all the blend films satisfying this criterion (Φ_q <60%) exhibited a strong CT band relative to the LE band. Figure S15 shows the decomposed PL spectra with two Gaussian functions. Subsequently, Φ_q was determined using the PL intensity of the LE band (Figure 3b). Note that spectral decomposition was not performed when Φ_q evaluated by the PL intensity of the whole spectrum was more than 60% because it had a less impact on Φ_q. Note that many blend films with Φ_q of more than 60% did not exhibit a clear CT band.

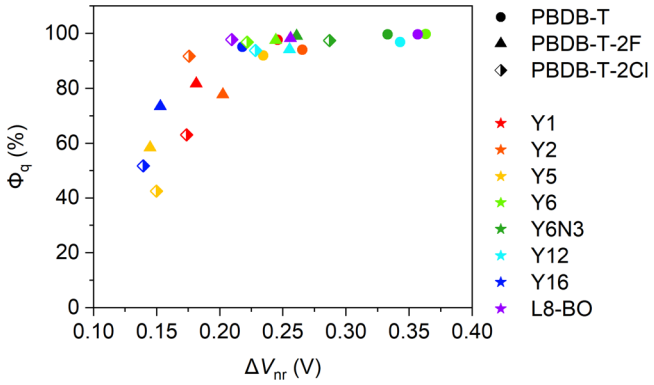

Figure S14. PL quenching yield Φ_q plotted against ΔV_{nr}. Φ_q was determined using the PL intensity of the entire spectrum.

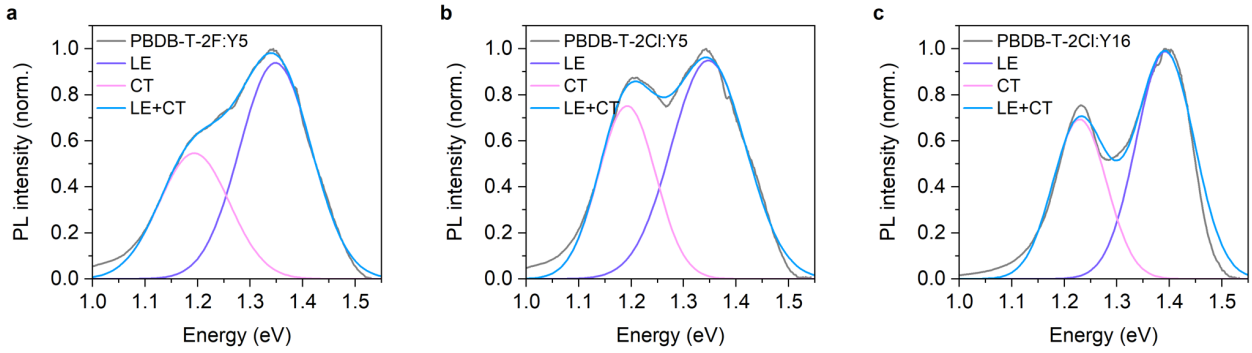

Figure S15. PL spectra of D:A blend films with Φ_q of less than 60% (grey lines). PL spectra were decomposed into two Gaussian functions. Φ_q was evaluated using the PL intensity of the LE band.

TA spectra of other inefficient PBDB-T-2F-based blends in the visible region

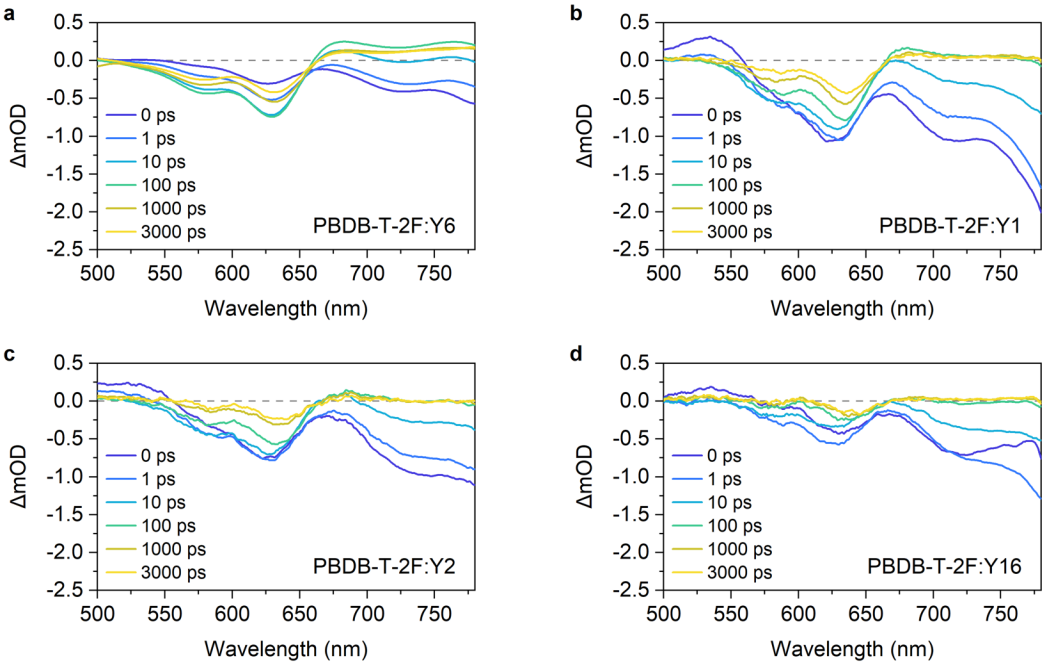

Figure S16. TA spectra of **a** PBDB-T-2F:Y6, **b** PBDB-T-2F:Y1, **c** PBDB-T-2F:Y2, and **d** PBDB-T-2F:Y16 blend films upon photoexcitation at 800 nm. The excitation fluences were 3.5 μJ cm^{-2} for the Y6 blend and 6.3 μJ cm^{-2} for the other blends. The experimental data for the Y6 blend film were obtained from our previous report.[S29]

Excitation-fluence dependence of the PBDB-T:Y5 blend

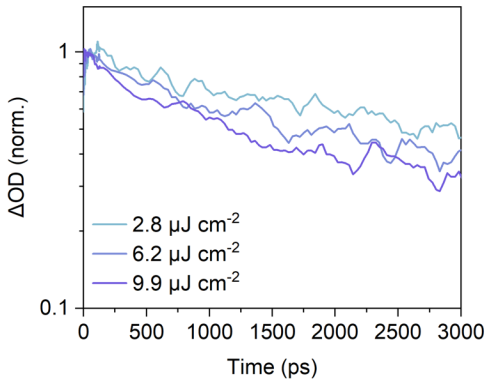

Figure S17. Excitation-fluence dependence of TA decays of the PBDB-T:Y5 blend film monitored at 630 nm.

Hole transfer rate

The charge transfer rate was calculated based on Marcus theory and is given as

$$k_{\mathrm{CT}} = \frac{2\pi}{\hbar}|J_{\mathrm{DA}}|^2 \frac{1}{\sqrt{4\pi k_{\mathrm{B}} T}} \exp\left(-\frac{\left(\Delta G^{\circ} + \lambda\right)^2}{4\lambda k_{\mathrm{B}} T}\right) \quad \text{(S10)}$$

where $\Delta G°$ (<0) is the energy difference between reactant and product, and λ is the reorganization energy.[S30,S31] J_{DA} is the electronic coupling strength and fixed at 0.02 eV in this study. Although we do not know the exact value of J_{DA}, this assumption is reasonable because hole transfer in the PBDB-T-2F:Y6 blend ($-\Delta G°$ = 0.12 eV) occurs on the sub-picosecond time scale.[S29,S32] In addition, we underline that the input J_{DA} value does not affect the relative charge transfer rate. Figure S18a shows the charge transfer rate calculated using Eq. S10 with various λ. Figure S18b shows the relative charge transfer rate, wherein the charge transfer rate at $-\Delta G°$ = 0.12 eV was normalized to 1. Because the IE difference between Y6 and Y5 was 0.12 eV, $-\Delta G°$ of the representative inefficient PBDB-T-2F:Y5 blend was expected to be approximately 0 eV. The relative rate remained an order of magnitude lower even when $-\Delta G°$ = 0 eV (of the order of 10^{11} s^{-1}), indicating that the hole transfer rate at the PBDB-T-2F:Y5 interface might be relatively fast as compared to the intrinsic lifetime of Y5 excitons.

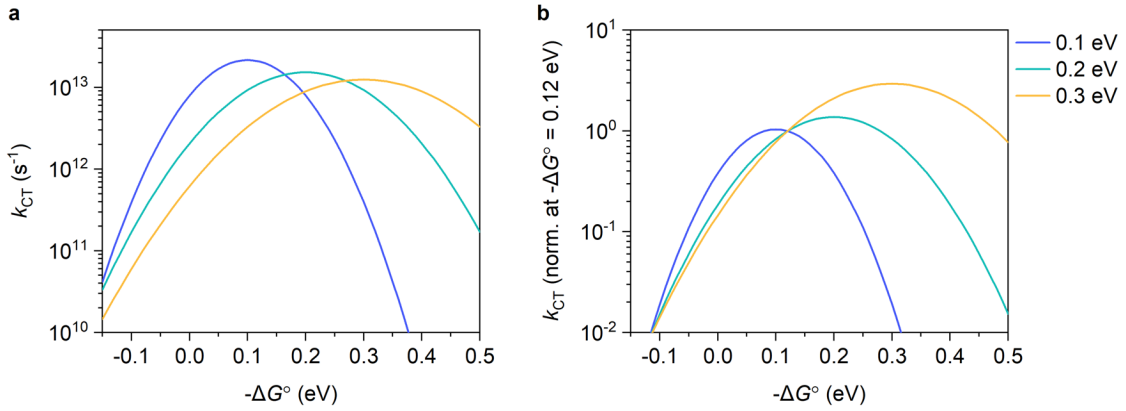

Figure S18. **a** Charge transfer rate calculated using Eq. S10 with various λ, as indicated. **b** Relative charge transfer rate where k_{CT} at $-\Delta G°$ = 0.12 eV was normalized to 1.

Fill factor

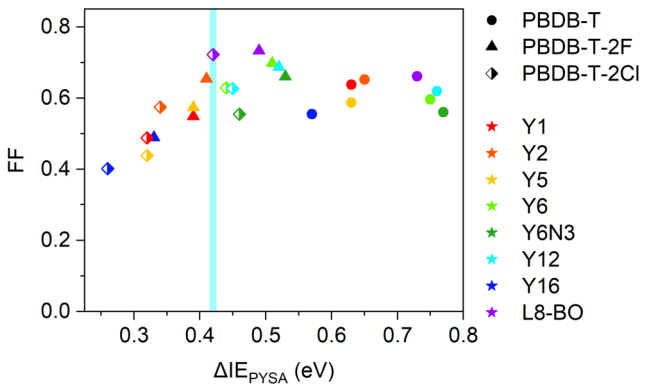

Figure S19. FF plotted against ΔIE_{PYSA}.

Device performances of ternary blend systems

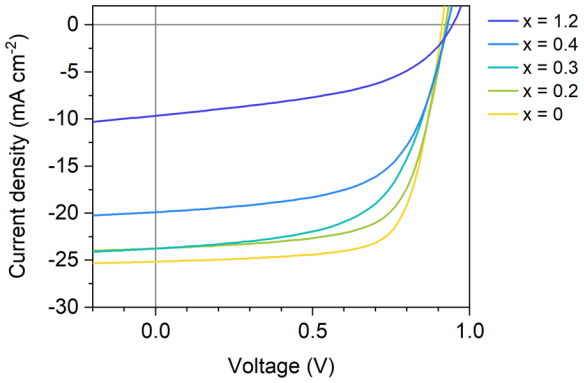

Figure S20. *J*–*V* characteristics of PBDB-T-2Cl:L8-BO:Y1 ternary blend devices. The blend ratio was 1:1.2−*x*:*x*.

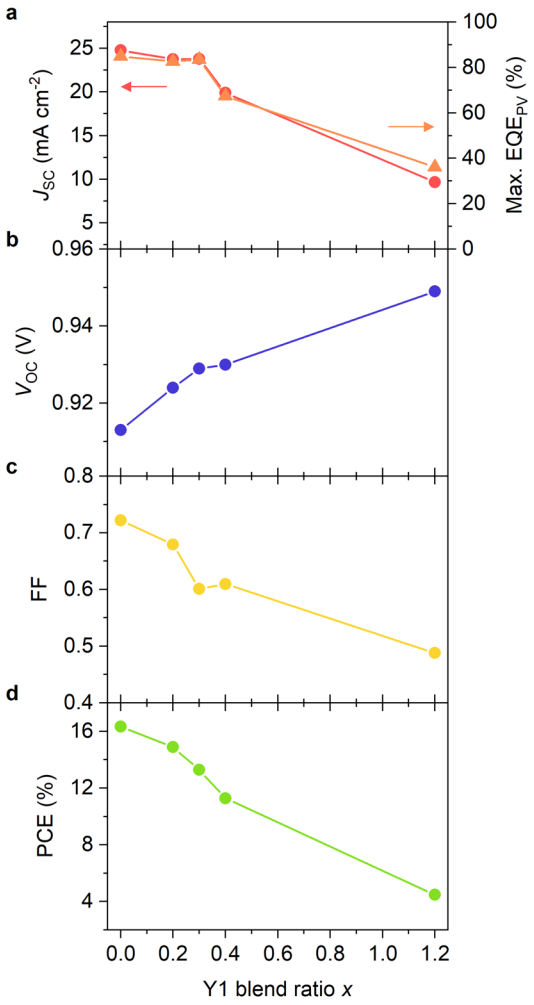

Figure S21. Parameters of PBDB-T-2Cl:L8-BO:Y1 ternary blend devices. The blend ratio was 1:1.2−*x*:*x*.

Table S9. Device parameters for PBDB-T-2Cl:L8-BO:Y1 ternary blend devices.

Y1 blend ratio	J_{SC} (mA cm^{-2})	J_{SC}^{calc} (mA cm^{-2})	V_{OC} (V)	FF	PCE (%)
0.2	23.75	23.80	0.924	0.679	14.88
0.3	23.77	24.29	0.929	0.601	13.28
0.4	19.90	19.31	0.930	0.609	11.28

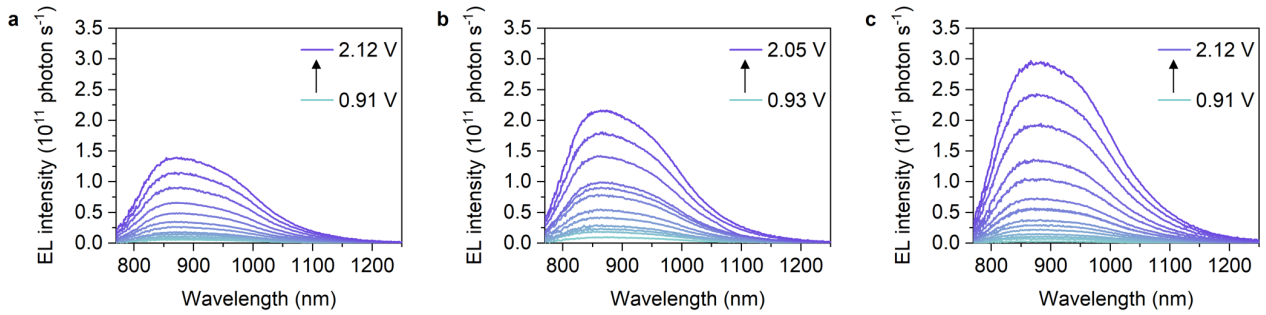

Figure S22. EL spectra of **a** PBDB-T-2Cl:L8-BO, **b** PBDB-T-2Cl:L8-BO:Y1 (1:1:0.2), and **c** PBDB-T-2Cl:Y1 devices.

Table S10. Charge generation efficiency and voltage loss.

	$EQE_{PV,max}$ [a] (%)	$\Delta V_{nr,calc}$ [b] (V)	$\Delta V_{nr,EL}$ [c] (V)
PBDB-T-2Cl:L8-BO	84.9	0.209	0.190
Ternary (1:1:0.2)	82.7	0.199	0.179
PBDB-T-2Cl:Y1	36.1	0.174	0.169

[a]: Maximum EQE_{PV} over the entire wavelength region.

[b]: ΔV_{nr} calculated by the procedure described in the Supplementary Information.

[c]: ΔV_{nr} calculated by the EQE_{EL} at $V = V_{JSC}$, at which the current density was equivalent to the J_{SC}. T was set to 296 K.

References

S1. J. Bertrandie, J. Han, C. S. P. De Castro, E. Yengel, J. Gorenflot, T. Anthopoulos, F. Laquai, A. Sharma and D. Baran, *Adv. Mater.*, 2022, **34**, 2202575.

S2. T. Saito, S.-i. Natsuda, R. Shirouchi, K. Imakita, K. Kohzuki and Y. Tamai, *Phys. Status Solidi A*, in press. DOI: 10.1002/pssa.202300121.

S3. S. Karuthedath, J. Gorenflot, Y. Firdaus, N. Chaturvedi, C. S. P. De Castro, G. T. Harrison, J. I. Khan, A. Markina, A. H. Balawi, T. A. D. Peña, W. Liu, R.-Z. Liang, A. Sharma, S. H. K. Paleti, W. Zhang, Y. Lin, E. Alarousu, D. H. Anjum, P. M. Beaujuge, S. De Wolf, I. McCulloch, T. D. Anthopoulos, D. Baran, D. Andrienko and F. Laquai, *Nat. Mater.*, 2021, **20**, 378-384.

S4. W. W. Li, K. H. Hendriks, A. Furlan, M. M. Wienk and R. A. J. Janssen, *J. Am. Chem. Soc.*, 2015, **137**, 2231-2234.

S5. K. Kawashima, Y. Tamai, H. Ohkita, I. Osaka and K. Takimiya, *Nat. Commun.*, 2015, **6**, 10085.

S6. J. Peet, J. Y. Kim, N. E. Coates, W. L. Ma, D. Moses, A. J. Heeger and G. C. Bazan, *Nat. Mater.*, 2007, **6**, 497-500.

S7. J. Hou, H.-Y. Chen, S. Zhang, G. Li and Y. Yang, *J. Am. Chem. Soc.*, 2008, **130**, 16144-16145.

S8. S. H. Park, A. Roy, S. Beaupré, S. Cho, N. Coates, J. S. Moon, D. Moses, M. Leclerc, K. Lee and A. J. Heeger, *Nat. Photonics*, 2009, **3**, 297-302.

S9. Y. Liang, Z. Xu, J. Xia, S.-T. Tsai, Y. Wu, G. Li, C. Ray and L. Yu, *Adv. Mater.*, 2010, **22**, E135-E138.

S10. G. Zhao, Y. He and Y. Li, *Adv. Mater.*, 2010, **22**, 4355-4358.

S11. E. Zhou, Q. Wei, S. Yamakawa, Y. Zhang, K. Tajima, C. Yang and K. Hashimoto, *Macromolecules*, 2010, **43**, 821-826.

S12. Z. Ma, E. Wang, K. Vandewal, M. R. Andersson and F. Zhang, *Appl. Phys. Lett.*, 2011, **99**, 143302.

S13. E. Wang, Z. Ma, Z. Zhang, K. Vandewal, P. Henriksson, O. Inganäs, F. Zhang and M. R. Andersson, *J. Am. Chem. Soc.*, 2011, **133**, 14244-14247.

S14. J. W. Jung, F. Liu, T. P. Russell and W. H. Jo, *Energy Environ. Sci.*, 2012, **5**, 6857-6861.

S15. J. Woong Jung, J. Woong Jo, F. Liu, T. P. Russell and W. Ho Jo, *Chem. Commun.*, 2012, **48**, 6933-6935.

S16. E. Zhou, J. Cong, K. Hashimoto and K. Tajima, *Energy Environ. Sci.*, 2012, **5**, 9756-9759.

S17. C. Cabanetos, A. El Labban, J. A. Bartelt, J. D. Douglas, W. R. Mateker, J. M. J. Fréchet, M. D. McGehee and P. M. Beaujuge, *J. Am. Chem. Soc.*, 2013, **135**, 4656-4659.

S18. L. Dou, C.-C. Chen, K. Yoshimura, K. Ohya, W.-H. Chang, J. Gao, Y. Liu, E. Richard and Y. Yang, *Macromolecules*, 2013, **46**, 3384-3390.

S19. X. Guo, N. Zhou, S. J. Lou, J. Smith, D. B. Tice, J. W. Hennek, R. P. Ortiz, J. T. L. Navarrete, S. Li, J. Strzalka, L. X. Chen, R. P. H. Chang, A. Facchetti and T. J. Marks, *Nat. Photonics*, 2013, **7**, 825-833.

S20. K. H. Hendriks, G. H. L. Heintges, V. S. Gevaerts, M. M. Wienk and R. A. J. Janssen, *Angew. Chem. Int. Ed.*, 2013, **52**, 8341-8344.

S21. I. Osaka, T. Kakara, N. Takemura, T. Koganezawa and K. Takimiya, *J. Am. Chem. Soc.*, 2013, **135**, 8834-8837.

S22. Y. Liu, J. Zhao, Z. Li, C. Mu, W. Ma, H. Hu, K. Jiang, H. Lin, H. Ade and H. Yan, *Nat. Commun.*, 2014, **5**, 5293.

S23. M. Wang, H. Wang, T. Yokoyama, X. Liu, Y. Huang, Y. Zhang, T.-Q. Nguyen, S. Aramaki and G. C. Bazan, *J. Am. Chem. Soc.*, 2014, **136**, 12576-12579.

S24. L. Ye, S. Zhang, W. Zhao, H. Yao and J. Hou, *Chem. Mater.*, 2014, **26**, 3603-3605.

S25. W. Yue, R. S. Ashraf, C. B. Nielsen, E. Collado-Fregoso, M. R. Niazi, S. A. Yousaf, M. Kirkus, H.-Y. Chen, A. Amassian, J. R. Durrant and I. McCulloch, *Adv. Mater.*, 2015, **27**, 4702-4707.

S26. M. Zhang, X. Guo, W. Ma, H. Ade and J. Hou, *Adv. Mater.*, 2015, **27**, 4655-4660.

S27. U. Rau, B. Blank, T. C. M. Müller and T. Kirchartz, *Phys. Rev. Appl.*, 2017, **7**, 044016.

S28. J. Yao, T. Kirchartz, M. S. Vezie, M. A. Faist, W. Gong, Z. He, H. Wu, J. Troughton, T. Watson, D. Bryant and J. Nelson, *Phys. Rev. Appl.*, 2015, **4**, 014020.

S29. S.-i. Natsuda, T. Saito, R. Shirouchi, Y. Sakamoto, T. Takeyama, Y. Tamai and H. Ohkita, *Energy Environ. Sci.*, 2022, **15**, 1545-1555.

S30. R. A. Marcus, *Rev. Mod. Phys.*, 1993, **65**, 599-610.

S31. Y. Tamai, *Aggregate*, 2022, **3**, e280.

S32. A. Karki, J. Vollbrecht, A. J. Gillett, S. S. Xiao, Y. Yang, Z. Peng, N. Schopp, A. L. Dixon, S. Yoon, M. Schrock, H. Ade, G. N. M. Reddy, R. H. Friend and T.-Q. Nguyen, *Energy Environ. Sci.*, 2020, **13**, 3679-3692.